AIAA 2001–2631

Higher-Order Aerodynamic Computations On Multi-Block Grids

S. De Rango and D. W. Zingg
Institute for Aerospace Studies
University of Toronto
4925 Dufferin St., Toronto, Ontario
M3H 5T6, Canada

15th AIAA Computational Fluid Dynamics Conference

11-14 June 2001/Anaheim, CA

Higher-Order Aerodynamic Computations On Multi-Block Grids

S. De Rango* and D. W. Zingg†
Institute for Aerospace Studies
University of Toronto
4925 Dufferin St., Toronto, Ontario
M3H 5T6, Canada

We investigate use of higher-order methods on multi-block grids with application to flow over high-lift multi-element airfoil configurations. The components of the spatial discretization, including the convective and viscous terms, the numerical boundary schemes, the numerical dissipation, and the integration technique used to calculate forces and moments, have all been raised to a level of accuracy consistent with third-order global accuracy. Numerical dissipation is added using matrix dissipation. Turbulence is modeled with the Spalart-Allmaras turbulence model. A grid convergence study is performed to evaluate the accuracy of the higher-order algorithm on multi-block grids. The results show that this globally higher-order approach can provide equivalent accuracy to a second-order algorithm on a grid with several times fewer nodes, thus greatly reducing the cost of computing flows over multi-element airfoils.

Introduction

Accurate modeling of the complex turbulent flow about high-lift multi-element airfoils is critical for the design of modern aircraft. The use of numerical solutions of the compressible Navier-Stokes equations with a turbulence closure model has resulted in a reasonable degree of success. Rumsey et al.[1] provide a thorough review of progress and issues in this area. One issue which remains a concern is the cost of computing accurate solutions. High-lift flows contain several flow features, such as regions of separated flow and confluent boundary layers, in which viscous effects are important. These flow features must be well resolved in order to simulate the flowfield accurately. Consequently, the grid densities required for accurate computation of multi-element flows greatly exceed those needed for single-element airfoils. Nelson et al.[2] showed that solutions for a three-element airfoil can have significant numerical error even using carefully designed grids with densities of over 100,000 points.

One means of reducing the cost of calculating multi-element airfoil flowfields is to use a higher-order spatial discretization. While it is relatively straightforward to demonstrate the advantages of higher-order methods in the context of model problems,[3–5] it can be more difficult to do so for practical problems on irregular grids. Nevertheless, several researchers have shown that computational costs can be reduced through the use of higher-order methods.[6–9] Through careful grid convergence studies, Zingg et al.[10] compared the accuracy of several spatial discretizations for the compressible Navier-Stokes equations, including the higher-order scheme of De Rango and Zingg,[11,12] a third-order upwind-biased differencing scheme with Roe's flux-difference splitting, and two second-order schemes. De Rango and Zingg raised the accuracy of the entire spatial discretization, including the boundary schemes, the viscous fluxes, and the grid metrics, to a level consistent with third-order global accuracy. With this discretization, the drag of a single-element airfoil can be computed with less than two percent numerical error using a grid with roughly 15,000 nodes. Three to four times as many nodes are needed to achieve the same accuracy using the other spatial discretizations tested.

The higher-order spatial discretization of De Rango and Zingg[11,12] was implemented in the well-known Navier-Stokes solver, ARC2D,[13] which is applicable to single-element airfoils. In this paper the higher-order discretization is implemented in TORNADO, a multi-block extension of ARC2D which uses the Spalart-Allmaras turbulence model. Descriptions and applications of TORNADO to various high-lift multi-element airfoil flows are given by Nelson et al.[2,14–16] and Godin at al.[17]

The purpose of the present paper is to describe the implementation of the higher-order discretization on multi-block grids and to demonstrate the resulting benefits in terms of reduced grid density requirements and improved efficiency in computing the flow over a high-lift three-element configuration.

*Graduate Student, stan@oddjob.utias.utoronto.ca.
†Professor, Member AIAA, dwz@oddjob.utias.utoronto.ca

Governing Equations and Numerical Method

The high-order spatial scheme has been implemented in the thin-layer Navier-Stokes solver TORNADO.[14,15] This solver uses a generalized curvilinear coordinate transformation and is applicable to multi-block structured grids. Convergence to steady state is achieved using the diagonal form of the Beam and Warming approximate-factorization algorithm with local time stepping. The effects of turbulence are modeled by the one-equation Spalart-Allmaras[19] model. Subiterations are used within the turbulence model. A circulation correction is used at the outer boundary.

In two-dimensional generalized coordinates, the thin-layer Navier-Stokes equations are given by

$$\partial_t \hat{Q} + \partial_\xi \hat{E} + \partial_\eta \hat{F} = \partial_\eta \hat{S} \tag{1}$$

where $\hat{Q}$ contains the conservative flow variables and $\hat{E}$ and $\hat{F}$ are the inviscid flux vectors in the ξ and η directions respectively. $\hat{S}$ contains the viscous terms.

Applying implicit Euler time-marching to the discretized form of Eq. 1 and linearizing, one obtains:

$$[I + h\delta_\xi \hat{A}^n + h\delta_\eta \hat{B}^n - h\mathcal{R}e^{-1}\delta_\eta \hat{M}^n]\Delta\hat{Q}^n = \hat{R} \tag{2}$$

where

$$\hat{R}^n = -h[\delta_\xi \hat{E}(\hat{Q}^n) + \delta_\eta \hat{F}(\hat{Q}^n) - \delta_\eta \hat{S}(\hat{Q}^n)] \tag{3}$$

The time-step is denoted by h, $\hat{Q}^n = \hat{Q}(nh)$, $\Delta\hat{Q}^n = \hat{Q}^{n+1} - \hat{Q}^n$, and δ denotes a generic spatial operator. The matrices $\hat{A}$, $\hat{B}$, and $\hat{M}$ are the flux Jacobians, defined by

$$\hat{A} = \frac{\partial \hat{E}}{\partial \hat{Q}}, \quad \hat{B} = \frac{\partial \hat{F}}{\partial \hat{Q}}, \quad \hat{M} = \frac{\partial \hat{S}}{\partial \hat{Q}} \tag{4}$$

The diagonalized, approximately-factored form of Eq. 2 is:

$$T_\xi[I + \delta_\xi \Lambda_\xi]\hat{N}[I + \delta_\eta \Lambda_\eta]T_\eta^{-1}\Delta\hat{Q}^n = \hat{R}^n \tag{5}$$

where

$$\hat{N} = T_\xi^{-1} T_\eta \tag{6}$$

The matrices Λ_ξ and Λ_η are diagonal matrices whose elements are the eigenvalues of the flux Jacobians, including a contribution from the viscous flux Jacobian.[13] The matrix T_ξ has the eigenvectors of $\hat{A}$ as columns and T_η has the eigenvectors of $\hat{B}$ as columns.

Higher-Order Spatial Discretization

Convective fluxes

Centered differences with added numerical dissipation are used for the convective fluxes. The numerical dissipation is added using the matrix dissipation scheme of Swanson and Turkel.[20] For subsonic flows, we do not require any first-order dissipation, and hence the numerical dissipation is third order. For transonic flows, we use the simple pressure switch described by Pulliam[13] to introduce a limited amount of first-order dissipation near shocks.

Gustafsson[21] has shown that the numerical boundary schemes can be one order lower than the interior scheme without reducing the global order of accuracy. Hence we can use second-order numerical boundary schemes while preserving third-order global accuracy. Nevertheless, we use third-order boundary schemes wherever possible. Note that the use of fourth-difference (third-order) dissipation necessitates the use of a five-point stencil and thus the solution of pentadiagonal systems. Increasing the accuracy of the centered difference operator to fourth order does not increase the stencil size, and the overall increase in computing expense per grid node is small. Finally, note that the grid metrics are evaluated using the same operators as the convective fluxes without any numerical dissipation.

The following operators are used to approximate first derivatives:

Interior (4th-order)

$$\delta_x q_j = \frac{1}{12\Delta x}(-q_{j+2} + 8q_{j+1} - 8q_{j-1} + q_{j-2}) \tag{7}$$

First Interior Node (3rd-order)

$$\delta_x q_j = \frac{1}{6\Delta x}(-2q_{j-1} - 3q_j + 6q_{j+1} - q_{j+2}) \tag{8}$$

Boundary (3rd-order)

$$\delta_x q_j = \frac{1}{24\Delta x}(-11q_j + 18q_{j+1} - 9q_{j+2} + 2q_{j+3}) \tag{9}$$

The last equation is required only for the calculation of grid metrics.

The following third-order operator is used for the numerical dissipation:

$$\frac{1}{\Delta x}(q_{j+2} - 4q_{j+1} + 6q_j - 4q_{j-1} + q_{j-2}) \tag{10}$$

The finite-difference stencil in Eq. 10 cannot be used at the first and last interior nodes. The following operator should be used to maintain third-order scaling for the dissipation at near-boundary nodes:

$$\frac{1}{\Delta x}(-q_{j-1} + 3q_j - 3q_{j+1} + q_{j+2}) \tag{11}$$

Viscous Fluxes

The viscous terms are in the following general form:

$$\partial_x(\alpha_j \partial_x \beta_j) \tag{12}$$

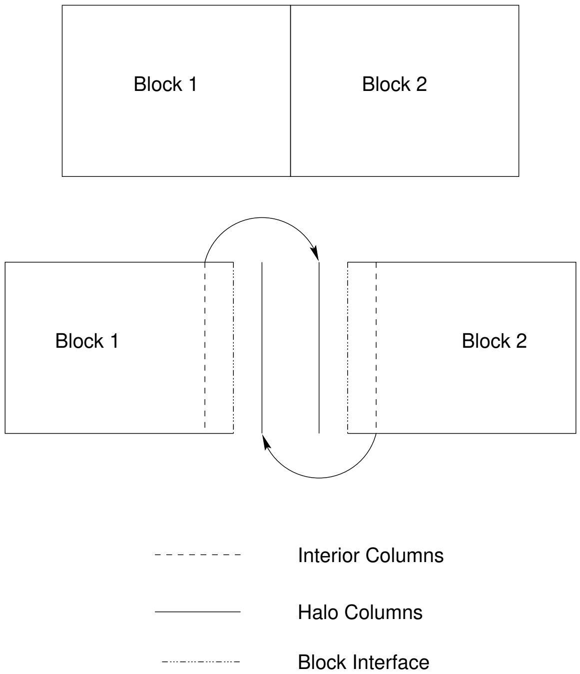

Fig. 1 Two-block grid with halo data

The following fourth-order expression is used to calculate the $\partial_x \beta_j$ term at half nodes:

$$(\delta_x\beta)_{j+\frac{1}{2}} = \frac{1}{24\Delta x}(\beta_{j-1} - 27\beta_j + 27\beta_{j+1} - \beta_{j+2}) \quad (13)$$

Near boundaries, the following third-order expression is used:

$$(\delta_x\beta)_{j+\frac{1}{2}} = \frac{1}{24\Delta x}(-23\beta_j + 21\beta_{j+1} + 3\beta_{j+2} - \beta_{j+3}) \quad (14)$$

The value of $\alpha_{j+\frac{1}{2}}$ is determined using the following fourth-order interpolation formula:

$$\alpha_{j+\frac{1}{2}} = \frac{1}{16}(-\alpha_{j-1} + 9\alpha_j + 9\alpha_{j+1} - \alpha_{j+2}) \quad (15)$$

Near boundaries, a third-order formula is used:

$$\alpha_{j+\frac{1}{2}} = \frac{1}{8}(3\alpha_j + 6\alpha_{j+1} - \alpha_{j+2}) \quad (16)$$

The complete operator is then found from:

$$\begin{aligned}\delta_x(\alpha_j\delta_x\beta_j) \quad = \quad & \frac{1}{24\Delta x}(\alpha_{j-3/2}(\delta_x\beta)_{j-3/2} \quad (17)\\ & -27\alpha_{j-1/2}(\delta_x\beta)_{j-1/2}\\ & +27\alpha_{j+1/2}(\delta_x\beta)_{j+1/2}\\ & -\alpha_{j+3/2}(\delta_x\beta)_{j+3/2})\end{aligned}$$

in the interior, and

$$\begin{aligned}\delta_x(\alpha_j\delta_x\beta_j) \quad = \quad & \frac{1}{24\Delta x}(-23\alpha_{j-1/2}(\delta_x\beta)_{j-1/2} \quad (18)\\ & +21\alpha_{j+1/2}(\delta_x\beta)_{j+1/2}\\ & +3\alpha_{j+3/2}(\delta_x\beta)_{j+3/2}\\ & -\alpha_{j+5/2}(\delta_x\beta)_{j+5/2})\end{aligned}$$

near boundaries. This approach leads to a seven-point stencil. On the left-hand-side of the approximate factorization algorithm, a second-order operator is used.

Turbulence Model

For the single-element cases presented in De Rango and Zingg,[11,12] the diffusive terms in the Spalart-Allmaras model were handled in the same manner as the viscous terms described in the preceding subsection. In TORNADO, the diffusive terms in the turbulence model are currently treated using the original second-order differences. A first-order upwind approximation for the convective terms in the turbulence model is used in order to maintain positivity of the eddy viscosity. Single-element results comparing the higher-order algorithm using the algebraic Baldwin-Lomax[22] and Spalart-Allamaras turbulence models indicate that the first-order convective terms do not introduce significant numerical error.[11]

Boundary Conditions

De Rango and Zingg[11] provide details concerning treatment of boundary conditions and integration of force coefficients.

Treatment of Block Interfaces

Neighbouring block boundaries, in the streamwise direction, are overlapped at the interfaces. A specified number of columns of points are taken from the neighbouring block (known as *halo* columns). Consider the rectangular 2-block grid in Fig. 1. For simplicity, only one *halo* column will be considered here. The first interior column of block 2 is stored in the *halo* column of block 1, and the last interior column of block

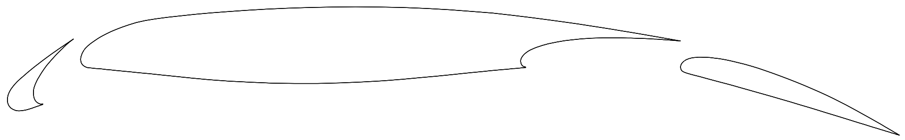

Fig. 2 High-lift test case A2

1 is stored in the *halo* column of block 2. Blocks 1 and 2 are then updated independently, resulting in two solutions at the block interface. The two interface solutions are subsequently averaged. At steady state, the streamwise interface is completely transparent. Common block interfaces in the cross-stream direction are treated like wake-cuts as described in De Rango and Zingg.[11]

Element	Upper Surface	Lower Surface
Slat	5.00	-
Main	0.97	11.0
Flap	2.70	99.3

Table 1 Transition locations given as percentage of elemental chord

Grid	Number of Nodes
A	255,295
B	183,721
C	126,125
D	72,837
E	51,749

Table 2 Grid densities

Results and Discussion

Overview of Test Case and Grid Details

The test case examined is Case A-2 from AGARD Advisory Report No. 303. Wind tunnel data were measured for a two-dimensional supercritical airfoil with high-lift devices and the model designation is NHLP 2D. These data were obtained during the 1970's as part of the National High Lift Programme in the United Kingdom. The case selected for examination here is L1T2 which includes a 12.5%c leading-edge slat and a 33%c single slotted flap, where c is the chord length of the nested configuration. The slat is located in the optimum position at an angle of 25 degrees and the flap angle is 20 degrees. This geometry, which is typical of a take-off configuration, is shown in Fig. 2. TORNADO results for this case were first presented by Nelson et al.[2]

The flow conditions for this case are $M_\infty = 0.197$, a Reynolds number of 3.52×10^6, and an angle of attack of 20.18°. The transition points are tabulated in Table 1. The transition for the lower surface of the slat is fixed to the third node from the sharp point between the slat leading and trailing edges as illustrated in Fig. 3.

In De Rango and Zingg,[12] grid convergence studies were carried out on 2D single-element airfoils using a family of three grids labeled A, B and C. Grid B was generated by removing every second node in both coordinate directions from grid A, and grid C was similarly generated from grid B. Grid C had practical density, suitable for use in three dimensions. Grids A and B were primarily for estimation of solution error. The results suggested that the solutions obtained on grid A (approx. 200,000 nodes) are almost grid independent, i.e., discretization errors are small on that grid. A superior discretization is one which produces a solution sufficiently close to the grid-independent solution on as coarse a grid as posssible. In particular, the goal was to obtain discretization errors below two percent on grid C. We follow a similar approach for the multi-element case examined here.

Five grids are used in this study, each of them generated independently with an H-mesh topology. Generating a sequence of grids suitable for multi-element cases in the fashion described above would make the grid density of a grid A impractical. The solution domain for each grid is divided into 27 blocks. The same domain decomposition is shared among all five grids and is shown in Fig. 4. The grids are labeled as grids A through E. The grid densities are given in Table 2. The far-field boundary is placed at a distance of 24 chords from the airfoil surface. Grid cells at the far-field boundaries are approximately 1 chord in length.

The slat requires special attention. At an angle of attack of 20.18°, the pressure gradients near the leading edge are quite large. In Nelson et al.,[2] it was shown that at high angles of attack, very high flow gradients exist outside the boundary layer near the leading edge of the slat. Hence, the streamwise point spacing near the leading edge of the slat is set to $2 \times 10^{-4}c$ on grids B through E. For grid A the spacing in this region is somewhat smaller. Trailing-edge clustering is set at $5 \times 10^{-4}c$ for all three elements and is kept constant for all of the grids. The spacing used is the smallest of those used in De Rango and Zingg[11,12] for single-element cases and is unlikely to introduce significant numerical error. The off-wall spacing is also kept constant for all five grids at 10^{-6} chords.

Test Case Results

Our goal is to obtain a solution on a grid of practical density like grid D (73,000 nodes) that is within two percent of the grid A solution. Grid E is included to provide an idea of how quickly the accuracy of the two discretization schemes deteriorates with coarser grids.

To ensure that the off-wall spacing of 10^{-6} chords is sufficiently small enough not to introduce significant numerical error, we introduce grid AA. Grid AA is identical to grid A except that the off-wall spacing is reduced to 5×10^{-7} chords. The higher-order results on grid A and AA are shown in Table 3. The difference between the two solutions is negligible, indicating that the original choice for the off-wall spacing is adequate. For all grids, the y^+ value at the first point from the surface is less than one, having a maximum of 0.8 on the main element for grid E.

Fig. 5 shows the grid convergence of the lift coefficient, C_l, the pressure drag coefficient, C_{d_p}, and the friction drag coefficient, C_{d_f}. The results are plotted vs $1/N$ where N is the total number of grid nodes. The errors in lift coefficient are small for both discretization algorithms, with the higher-order scheme being more accurate than the second-order scheme on grids D and E. The errors in the drag components are much larger. Compared to the solution on grid A, the error in pressure drag for the higher-order scheme on grid D is less than 3% while the error in the second-order results for both pressure and friction drag coefficents on grid D exceeds 12%. The error in the drag components for the second-order scheme approaches 22% on grid E while the error in the higher-order result is still well behaved at approximately 5%.

The errors in the drag components of the individual elements of the high-lift configuration are given in Tables 5 and 6. The errors are determined relative to the values on grid A presented in Table 4. A benefit of analyzing the data in this manner is that it provides some insight into which areas of the grid need to be refined if further improvement in accuracy is desired. The pressure-drag error on the slat and main element for the second-order solution is quite large. The elemental pressure- and friction-drag error for the higher-order solution is several times smaller than those produced by the second-order algorithm.

Fig. 6 shows the experimental and computed surface pressure distributions for the NHLP airfoil. The computed result, using the second-order scheme on grid A, is very accurate, comparable to those presented by Nelson et al.,[2] using a somewhat different grid configuration. A portion of the upper surface pressure distribution of the slat is shown in Fig. 7. The second-order scheme, on grid D, does poorly at computing the minimum pressure. Similar results are found on the main element as well.

Fig. 8 shows boundary-layer velocity profiles at the trailing edge of the flap. For the second-order solution on grid A, every third grid point is plotted. The profiles can be divided into four regions:

1. the first 3% of chord above the flap surface corresponds to the flap boundary layer;
2. the region between 3% and 10% of chord corresponds to the wake from the main element;
3. the region between 10% and 18% of chord corresponds to the wake from the slat;
4. beyond 18% of chord above the flap surface, the flow slowly returns to free-stream conditions

Given the superior results obtained using the higher-order scheme for single-element cases,[10,12] the higher-order result on grid A is taken as the reference solution. Region 1 appears to be adequately resolved for both discretization schemes, even on grid D. In region 2, the higher-order result on grid D is more accurate than the second-order result on grid A, a grid with more than 3 times as many nodes. In region 3, the error in the second-order result on Grid D is quite large and increases in region 4. These slower velocities in the wake explain the larger drag values reported earlier. The second-order result on grid A and the higher-order result on grid D provide similar accuracy in regions 3 and 4. The second-order grid A result is slightly better in region 3 while the higher-order grid D result is slightly better in region 4. Nonetheless, the higher-order scheme is in excellent agreement with the reference solution using a grid with only 73,000 nodes, one third of the grid density of grid A.

Convergence rate and computational efficiency

Density residual and drag convergence histories for grid D, are displayed in Fig. 9. The two algorithms converge similarly for the first four orders of magnitude reduction in residual, and the higher-order algorithm converges somewhat more slowly after that. In general, for single-element cases, the lift and drag convergence for the two discretizations are quite similar. In this multi-element case, however, the higher-order scheme takes approximately 33% more iterations than the second-order scheme to converge to within 0.2% of the converged drag. The higher-order algorithm, however, produces a solution that is far more accurate on grid D with the second-order scheme requiring at least 3 times as many nodes to produce similar accuracy.

The added computational cost of the higher-order scheme in TORNADO is similar to the added cost in ARC2D. Compared to the second-order algorithm, the cost per grid node per iteration is increased by about 7%, with no increase in memory usage. This is an important factor when considering extending TORNADO to 3D applications. The higher-order scheme produces accurate results on relatively coarse grids,

Grid	C_l	C_{d_p}	C_{d_f}
AA	4.074	0.04398	0.01070
A	4.074	0.04393	0.01068

Table 3 Results for grids AA and A

Drag Component	Higher-order			Second-order		
	Slat	Main Element	Flap	Slat	Main Element	Flap
C_{d_p}	-0.71975	0.54096	0.22272	-0.71929	0.54082	0.22311
C_{d_f}	0.00196	0.00683	0.00189	0.00193	0.00672	0.00184

Table 4 Elemental drag components on grid A

Algorithm	Slat	Main Element	Flap	Complete Airfoil
higher-order	2.9	5.1	2.3	10.3
second-order	98.9	-34.7	-8.8	55.4

Table 5 Elemental pressure drag error in counts on grid D (Note: One count is equivalent to 0.0001 units in drag. The count errors are relative to the solution of each respective algorithm on grid A - see Table 4)

Algorithm	Slat	Main Element	Flap	Complete Airfoil
higher-order	0.2	-0.3	-0.5	-0.6
second-order	-1.0	-8.6	-3.9	-13.5

Table 6 Elemental friction drag error in counts on grid D (Note: The count errors are relative to the solution of each respective algorithm on grid A - see Table 4)

thereby reducing memory requirements and computational costs. Table 7 summarizes the memory requirements of TORNADO for the grid densities used in this study. The higher-order scheme produces results on grid D within approximately two percent of the solutions on grid A while only using 34 megabytes of memory.

Conclusions

A grid convergence study has been used to demonstrate that the higher-order discretization produces a substantial reduction in the numerical errors in multi-element airfoil flowfields in comparison with the second-order algorithm. The higher-order algorithm produces a smaller error on a given grid than the second-order algorithm produces on a grid with several times as many nodes. Hence it provides equivalent accuracy with a large reduction in computing expense. For example, using the higher-order discretization, numerical errors of less than 2 – 3% can be obtained in the computation of lift and drag components for a three-element airfoil using grids with roughly 73,000 nodes.

Acknowledgments

This research was supported by the Natural Sciences and Engineering Research Council of Canada and Bombardier Aerospace.

References

[1]Rumsey, C.L., Gatski, T.B., and Ying, S.X., "Prediction of High-Lift Flows Using Turbulent Closure Models," *AIAA J.*, Vol. 36, No. 5, May 1998, pp. 765-774.

[2]Nelson, T.E., and Godin, P., and De Rango, S., and Zingg, D.W., "Flow Computations For A Three-element Airfoil System," *CASI J.*, vol. 45, pp. 132–139, June 1999.

[3]Kreiss, H.-O., and Oliger, J., "Comparison of Accurate Methods for the Integration of Hyperbolic Equations," *Tellus*, vol. 24, 1972, pp. 199–215.

[4]Swartz, B., and Wendroff, B., "The Relative Efficiency of Finite Difference and Finite Element Methods," *SIAM J. Num. Anal.*, vol. 11, no. 5, 1974, pp. 979–993.

[5]Zingg, D.W., "Comparison of High-Order and Optimized Finite-Difference Methods for Simulating Linear Wave Phenomena," *SIAM J. Sci. Comput.*, Vol. 22, No. 2, 2000, pp. 476-502.

[6]Visbal, M.R., and Gaitonde, D.V., "High-Order-Accurate Methods for Complex Unsteady Subsonic Flows," *AIAA J.*, Vol. 37, No. 10, 1999, pp. 1231-1239.

[7]Rai, M.M., "Navier-Stokes Simulations of Rotor-Stator Interaction Using Patched and Overlaid Grids," *AIAA J. of Propulsion and Power*, Vol. 3, No. 5, 1987, pp. 387-396.

[8]Treidler, E.B., Ekaterinaris, J., and Childs, R.E., "Efficient Solution Algorithms for High-Accuracy Central Difference CFD Schemes," AIAA Paper 99-0302, Jan. 1999.

[9]Rai, M.M., and Chakravarty, S.R., "Conservative High-Order-Accurate Finite-Difference Methods for Curvilinear Grids," AIAA Paper 93-3380, June 1993.

[10]Zingg, D.W., and De Rango, S., and Nemec, M., and Pulliam, T.H., "Comparison of Several Discretizations for the Navier-Stokes Equations," *J. Comp. Phys.*, vol. 160, pp. 683–704, 2000.

[11]De Rango, S., and Zingg, D.W., "Aerodynamic Computations Using a Higher-Order Algorithm." AIAA Paper 99-0167, January 1999.

Grid	Number of Nodes	Memory Used (megabytes)
A	255,295	102
B	183,721	75
C	126,125	54
D	72,837	34
E	51,749	26

Table 7 Memory requirements for TORNADO

[12] De Rango, S., and Zingg, D.W., "Further Investigation of a Higher-Order Algorithm for Aerodynamic Computations." AIAA Paper 2000-0823, January 2000.

[13] Pulliam, T. H., "Efficient Solution Methods for the Navier-Stokes Equations." Lecture Notes For The von Karman Institute, for Fluid Dynamics Lecture Series: *Numerical Techniques For Viscous Flow Computation In Turbomachinery Bladings*, von Karman Institute, Brussels, Belgium, Jan. 1986.

[14] Nelson, T. E., Zingg, D. W., and Johnston, G. W., "Compressible Navier-Stokes Computations of Multielement Airfoil Flows Using Multiblock Grids," *AIAA Journal*, vol. 32, March 1994.

[15] Nelson, T. E., Zingg, D. W., and Johnston, G. W., "Navier-Stokes Computations for Multi-element Airfoils at Transonic Speeds," in *Proc. CFD 94*, pp. A1–01(1) to A1–01(8), CFD Society of Canada, 1994.

[16] Nelson, T.E., and Godin, P., and Zingg, D.W., "Multi-Element Airfoil Computations with One-Equation Turbulence Models." AIAA Paper 95-0357, January 1995.

[17] Godin, P., and Zingg, D.W., and Nelson, T.E., "High-Lift Aerodynamics Computations with One- and Two-Equation Turbulence Models," *AIAA Journal*, vol. 35, Feb. 1997.

[18] Frew, K., Zingg, D.W., and De Rango, S., "On Artificial Dissipation Models for Viscous Airfoil Computations," *AIAA Journal*, vol. 36, pp. 1732–1734, September 1998.

[19] Spalart, P. R., and Allmaras, S. R., "A One-Equation Turbulence Model for Aerodynamic Flows." AIAA Paper 92-0439, January 1992.

[20] Swanson, R.C., and Turkel, E., "On Central-Difference and Upwind Schemes," *J. Comp. Phys.*, vol. 101, pp. 292–306, 1992.

[21] Gustafsson, B., "The Convergence Rate for Difference Approximations to Mixed Initial Boundary Value Problems," *Math. Comp.*, vol. 29, no. 130, pp. 396–406, 1975.

[22] Baldwin, B., and Lomax, H., "Thin-Layer Approximation and Algebraic Model for Separated Turbulent Flows." AIAA Paper 78-257, January 1978.

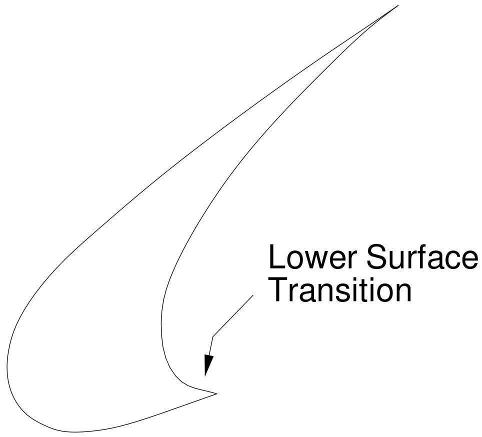

Fig. 3 Location of fixed transition point on lower surface of slat

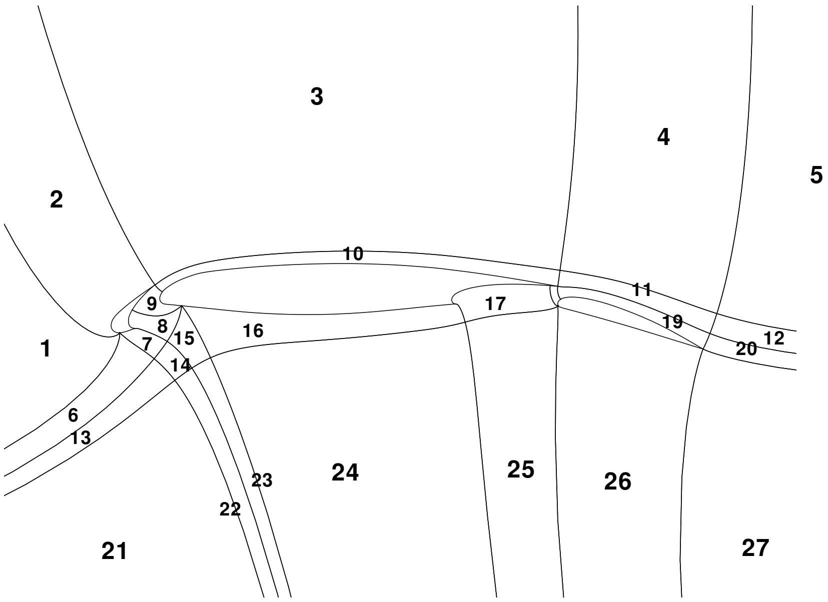

Fig. 4 Multi-block decomposition

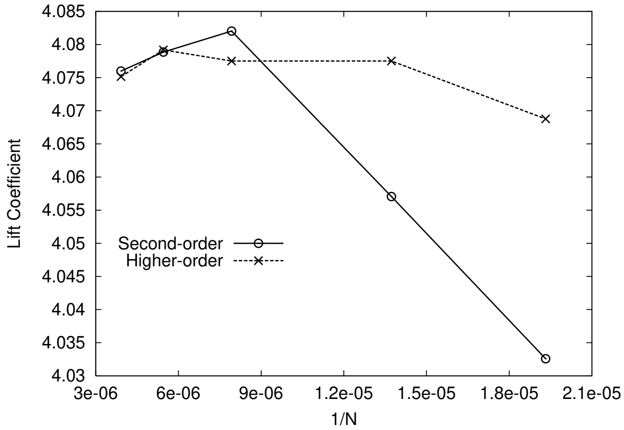

a) C_l

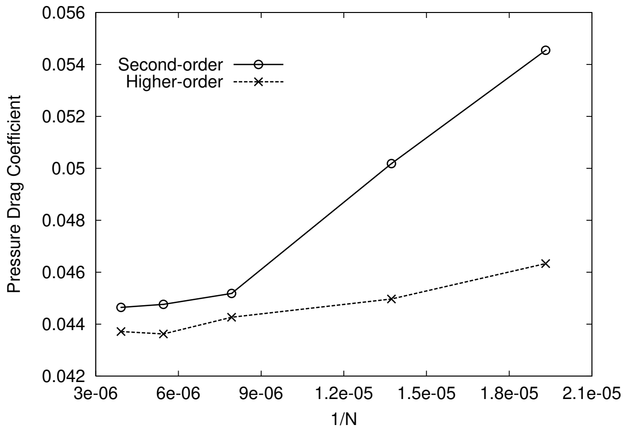

b) C_{d_p}

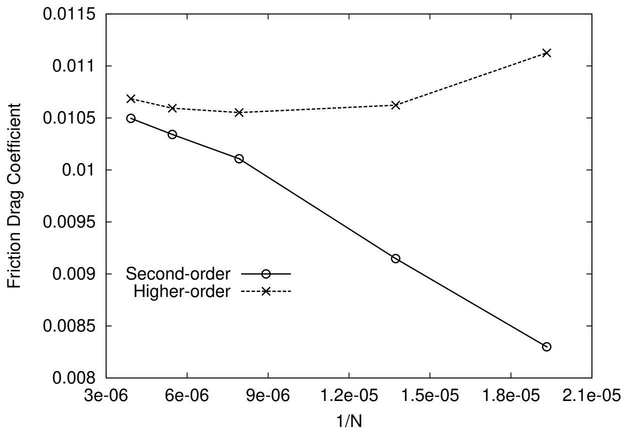

c) C_{d_f}

Fig. 5 Grid convergence study

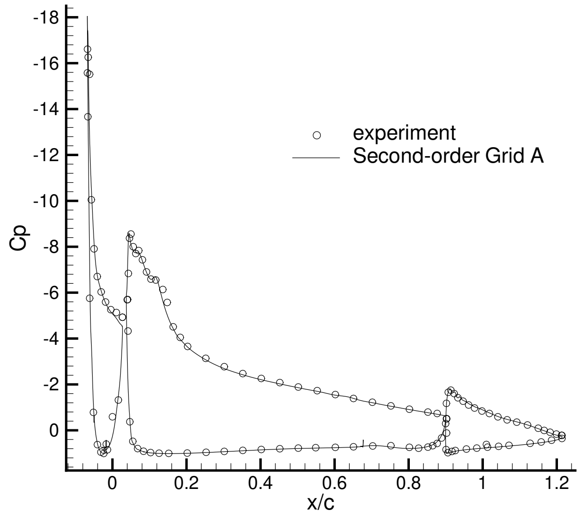

Fig. 6 Pressure distribution for the NHLP 2D configuration L1T2

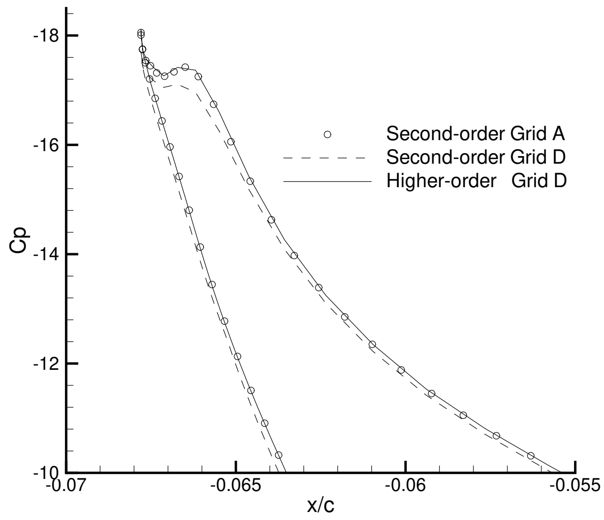

Fig. 7 Pressure distribution on upper surface of slat

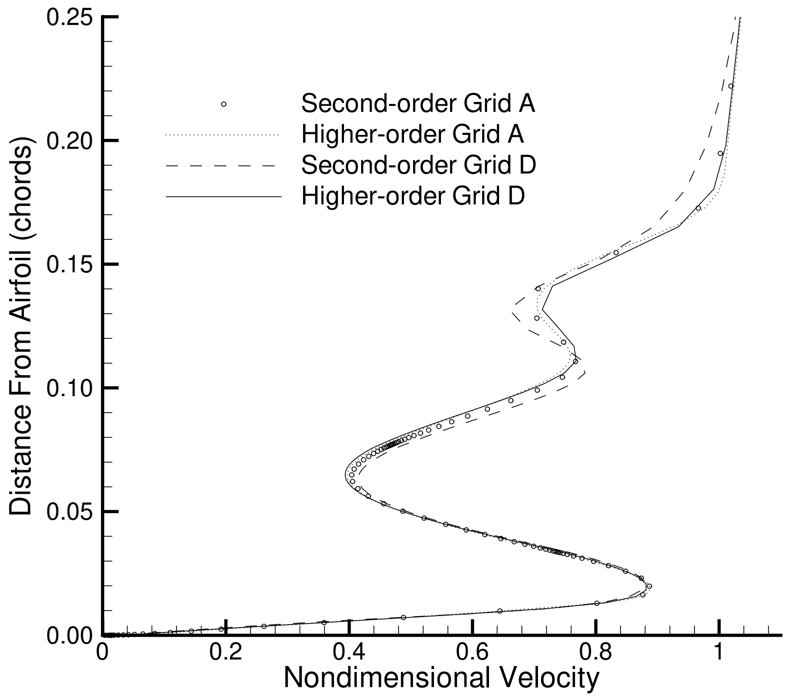

Fig. 8 Boundary-layer profile, upper surface of flap at trailing edge

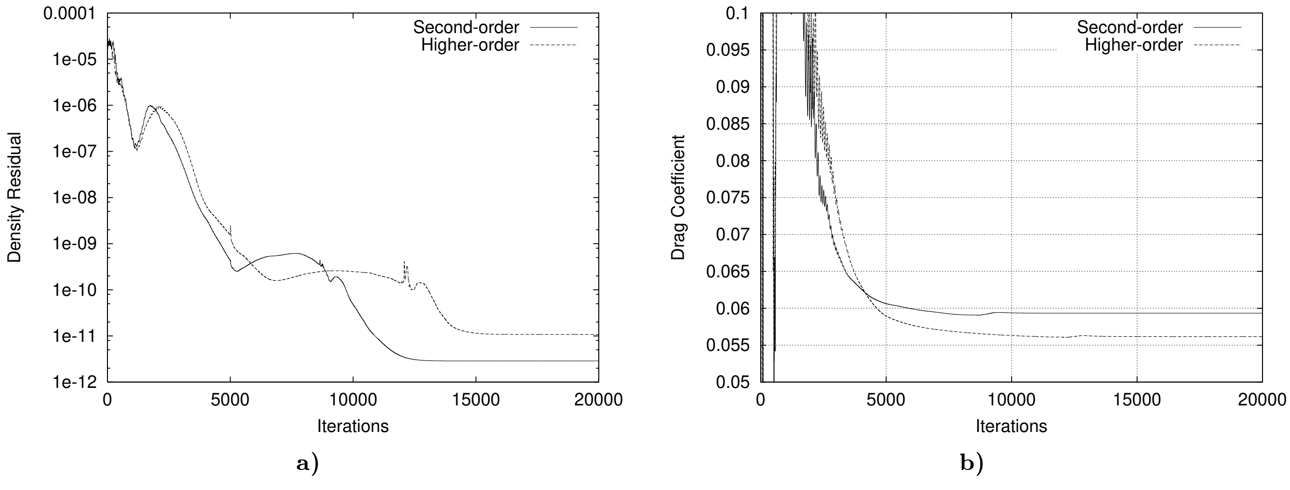

Fig. 9 Density residual and drag convergence history on grid D